J. Fluid Mech. (1983), *vol.* 135, *pp.* 71–94
Printed in Great Britain

Nonlinear focusing of surface waves by a lens – theory and experiment

By JAKOB J. STAMNES, ODD LØVHAUGEN, BJØRN SPJELKAVIK,
Central Institute for Industrial Research, P.O. Box 350, Blindern, Oslo 3, Norway

CHIANG C. MEI, EDMOND LO AND DICK K. P. YUE
Department of Civil Engineering, Massachusetts Institute of Technology, Cambridge, Massachusetts 02139, U.S.A.

(Received 5 January 1983 and in revised form 1 June 1983)

One of the recent developments in harnessing wave energy is to construct a line of submerged structures parallel to the incident swell crests in order to transform the straight crests to circular crests converging to a focus. To understand the neighbourhood of the focus, we have carried out theoretical studies by accounting for diffraction and nonlinearity, both separately and jointly. Experiments have also been conducted in a large outdoor basin and are compared with the theories. These comparisons tend to favour the approximate nonlinear theory, but the efficiency of the focusing device as an energy concentrator does not appear to be significantly impaired by nonlinear effects.

1. Introduction

The motivation for the work described in this paper stems from our effort to focus ocean swells for power-production purposes. In order to determine the feasibility of this idea, experiments have been carried out in an outdoor man-made basin at Elnes, 40 km north of Oslo. The basin has a depth of 3 m, a length of 150 m and a width of 100 m.

A typical set-up for a focusing experiment is illustrated in figure 1. Figure 1 (*a*) shows a photograph of the test basin during an experiment, and figure 1 (*b*) shows schematically the set-up discussed in this paper. A wave generator produces a diverging circular wave that is incident upon a lens for water waves. The lens has the ability to transform the diverging circular wave coming from the generator into a converging circular wave with focal point at a distance z_0 behind the lens. The wavelength is typically around 1 m in the experiments. In the experiment discussed in this paper, the width of the lens is 33.17 m, the distance from the wave generator to the lens is 60 m, and the distance from the lens to the geometrical focal point is $z_0 = 60$ m.

Lenses for water waves may consist of submerged structures. The functioning and construction of such lenses are described in Mehlum & Stamnes (1978); Løvhaugen (1981*a*); Heier (1981), and the details of the experimental procedure and signal processing are given in Løvhaugen (1981*b*). For our present purposes it suffices to say that the wave experiences a phase change as it passes over the lens, and the lens is constructed so as to give a non-uniform phase change which transforms a diverging wave to a converging wave. The mathematical model used to calculate the phase

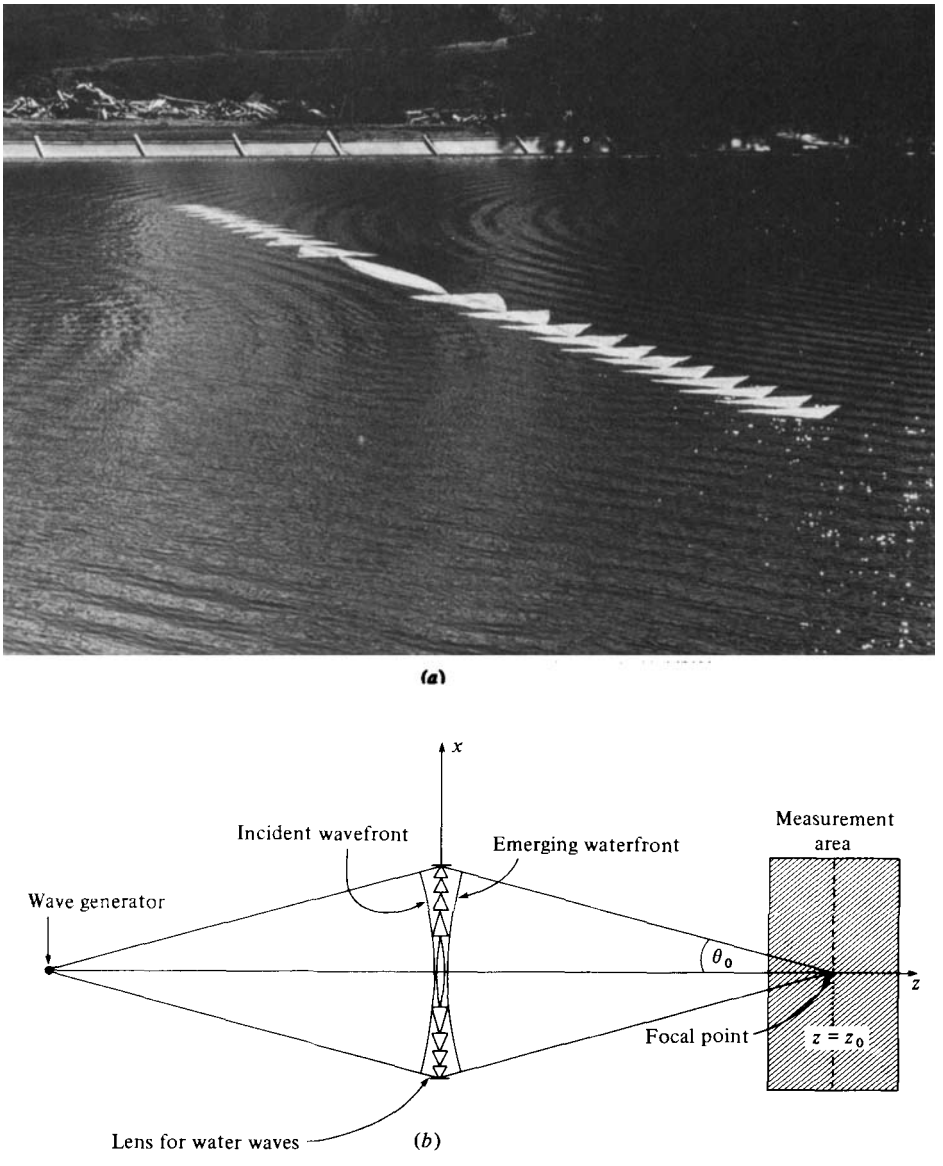

FIGURE 1. Illustration of a wave-focusing experiment. (*a*) is a photograph of a part of the test basin showing the wave as it passes over the lens during an experiment (Photo: NTB). (*b*) shows the geometry of the experiment discussed in the text. The focal distance is $z_0 = 60$ m, the width of the lens is $2a = 33.17$ m, and the measurement area is 20×40 m^2. The wavelength used in the experiment is $\lambda = 1$ m, which gives a value of $\sigma^2 = 28.805$ (cf. (2.9)).

change of a lens element as a function of its depth, size and shape is presented in Mehlum (1980).

Recently, methods have been developed that are suitable for studying water waves in focal regions within the framework of linear theory (Stamnes 1981; Stamnes, Ljunggren & Spjelkavik 1981). The results of these methods have been compared with

experimental results obtained at the Elnes test facilities. As long as the amplitude of the wave produced by the generator is relatively small one finds good agreement between the results of the linear theory and those of experiments (Løvhaugen 1981*a*; Heier 1981).

As the amplitude of the wave that is incident upon the lens increases, nonlinear effects start to play a role in the focal region. In order to determine how the nonlinear effects influence the energy distribution of the waves in the focal region, one needs a theory of nonlinear propagation of water waves that applies to focusing. A general nonlinear theory of this kind has not yet been developed. However, for small convergence angles it is possible to apply a nonlinear theory, based on a cubic Schrödinger equation, which may be solved numerically at a surprisingly moderate computing effort. The main objective of this paper is to compare the results of this theory with those obtained experimentally at the Elnes test facilities.

The paper is organized as follows. In §2 the exact linear theory and its parabolic approximation are given. The latter is shown to be quite accurate even for a rather large convergence angle corresponding to the experimental set-up at Elnes. The basic results of the nonlinear parabolic theory are presented in §3, and the results of the nonlinear theory in its linear limit are compared with those of the linear parabolic theory in §2. In §4 we decompose the wave field at lines parallel to the lens into a superposition of plane waves, and show how the amplitude of each individual plane-wave component in the nonlinear theory evolves with increasing distance from the lens to the line of observation. A description of the experiment and the processing of the experimental data is given in §5, and comparisons of results of linear and nonlinear theories with those of experiments are presented in §6. The main results of the paper are summarized in §7.

2. Exact linear theory and its parabolic approximation

Within the linear theory of wave propagation in water of constant depth we may assume that the amplitude $\eta(x, z)$ of the free-surface displacement

$$\mathrm{Re}\{\eta(x, z)\exp(-\mathrm{i}\omega t)\}$$

satisfies the two-dimensional Helmholtz equation

$$\left(\frac{\partial^2}{\partial x^2}+\frac{\partial^2}{\partial z^2}+k^2\right)\eta(x, z)=0, \tag{2.1}$$

whose solution may be written either in terms of an impulse-response integral or an angular-spectrum representation, i.e.

$$\eta(x, z)=-\frac{k}{2\mathrm{i}}\int_{-\infty}^{\infty}\eta(x', 0)\frac{z}{r}H_1^{(1)}(kr)\,\mathrm{d}x' \tag{2.2a}$$

$$=\frac{1}{2\pi}\int_{-\infty}^{\infty}\tilde{\eta}(k_x, z)\exp[\mathrm{i}k_x x]\,\mathrm{d}k_x, \tag{2.2b}$$

where $H_1^{(1)}(kr)$ is the first-order Hankel function of the first kind, $k=2\pi/\lambda$, λ being the wavelength, and

$$r=[(x-x')^2+z^2]^{\frac{1}{2}}, \tag{2.3}$$

$$\tilde{\eta}(k_x, z)=\tilde{\eta}(k_x, 0)\exp[\mathrm{i}(k^2-k_x^2)^{\frac{1}{2}}z]. \tag{2.4a}$$

Note that $\tilde{\eta}(k_x, 0)$ is the angular spectrum of plane waves propagating in the direction $\boldsymbol{k} = (k_x, (k^2 - k_x)^{\frac{1}{2}})$ into the half-plane $z > 0$. Since

$$\eta(x, z) = \frac{1}{2\pi} \int_{-\infty}^{\infty} \tilde{\eta}(k_x, z_0) \exp\{\mathrm{i}[k_x x + (k^2 - k_x^2)^{\frac{1}{2}}(z - z_0)]\} \, \mathrm{d}k_x, \tag{2.4b}$$

$\tilde{\eta}(k_x, z_0)$ is the angular spectrum of plane waves propagating into the half-plane $z > z_0$. It follows from (2.2*b*) that the angular spectrum $\tilde{\eta}(k_x, z)$ is the Fourier transform of the field, i.e.

$$\tilde{\eta}(k_x, z) = \int_{-\infty}^{\infty} \eta(x, z) \exp[-\mathrm{i}k_x x] \, \mathrm{d}x. \tag{2.4c}$$

The boundary value $\eta(x, 0)$ pertaining to a wave of unit amplitude that converges to a focal point at $(0, z_0)$, as illustrated in figure 1 (*b*), is given by

$$\eta(x, 0) = \eta_0 \exp[-\mathrm{i}kr_0], \quad r_0 = (x^2 + z_0^2)^{\frac{1}{2}} \tag{2.5}$$

within the aperture of the lens. Equations (2.2)–(2.5) constitute what we shall here denote the exact linear theory of focusing. A thorough discussion of this theory and examples of its application may be found in Stamnes (1981) and Stamnes *et al.* (1981), along with algorithms for efficient computation of the integrals in (2.2) and (2.4*b*).

The parabolic approximation pertains to the case of small angles of convergence, i.e. θ_0 in figure 1 (*b*) is small. Then the Helmholtz equation may be simplified by substituting the ansatz

$$\eta(x, z) = A(x, z) \exp(\mathrm{i}kz) \tag{2.6}$$

into (2.1) and neglecting the term $\partial^2 A / \partial z^2$, since $A(x, z)$ is supposed to vary slowly in the z-direction. As a result we obtain the so-called parabolic wave equation

$$\frac{\partial A}{\partial z} - \frac{\mathrm{i}}{2k} \frac{\partial^2 A}{\partial x^2} = 0. \tag{2.7}$$

We now introduce scaled coordinates

$$X = \frac{x}{a}, \quad Z = \frac{z}{z_0}, \tag{2.8}$$

where $2a$ is the width of the lens. Equation (2.7) then becomes

$$\frac{\partial A}{\partial Z} - \frac{\mathrm{i}}{2\sigma^2} \frac{\partial^2 A}{\partial X^2} = 0, \quad \sigma^2 = \frac{ka^2}{z_0}. \tag{2.9}$$

The parameter σ should be of order unity for the parabolic approximation to be valid. The solution of (2.9) is given by

$$A(X, Z) = \frac{1}{2\pi} \int_{-\infty}^{\infty} \tilde{A}(f_X, Z) \exp[\mathrm{i}f_X X] \, \mathrm{d}f_X, \tag{2.10a}$$

where

$$\tilde{A}(f_X, Z) = \tilde{A}(f_X, 0) \exp\left(-\frac{\mathrm{i}f_X^2 Z}{2\sigma^2}\right), \tag{2.10b}$$

with

$$\tilde{A}(f_X, Z) = \int_{-\infty}^{\infty} A(X, Z) \exp[-\mathrm{i}f_X X] \, \mathrm{d}X. \tag{2.10c}$$

Using the convolution theorem we may write (2.10*a*) in the form of an impulse-response integral, i.e.

$$A(X,Z) = \int_{-\infty}^{\infty} A(X',0)\,G(X-X',Z)\,\mathrm{d}X', \tag{2.11a}$$

where

$$G(X,Z) = \frac{1}{2}\int_{-\infty}^{\infty} \exp\left[\mathrm{i}\left(f_X X - \frac{f_X^2}{2\sigma^2}Z\right)\right]\mathrm{d}f_X$$

$$= \frac{\sigma}{(2\pi Z)^{\frac{1}{2}}}\exp\left[\mathrm{i}\left(\frac{\sigma^2 X^2}{2Z} - \frac{\pi}{4}\right)\right]. \tag{2.11b}$$

In the parabolic approximation the boundary value (2.5) becomes (cf. (2.6) and (2.8))

$$A(X,0) = A_0 \exp\left[-\tfrac{1}{2}\mathrm{i}\sigma^2 X^2\right]. \tag{2.12}$$

The importance of imposing the parabolic approximation not only on the angular spectrum (cf. (2.10*b*)) or the impulse response (cf. (2.11*b*)), but also on the boundary value (2.12), has been pointed out recently (Southwell 1981).

We consider two different focusing geometries. In the first case (case I) the lens is assumed to fill an opening in a breakwater. The appropriate boundary value then is

$$A^{\mathrm{I}}(X,0) = A_0\begin{cases}\exp\left[-\tfrac{1}{2}\mathrm{i}\sigma^2(X^2-1)\right] & (|X| \leqslant 1),\\ 0 & (|X| > 1),\end{cases} \tag{2.13}$$

which represents approximately a circular crest of unit amplitude having zero phase at $|X| = 1$.

In the other case (case II) the lens is surrounded by deep water, so that we have

$$A^{\mathrm{II}}(X,0) = \begin{cases}A^{\mathrm{I}}(X,0) & (|X| \leqslant 1),\\ A_0 & (|X| > 1).\end{cases} \tag{2.14}$$

Substitution of (2.13) and (2.14) in (2.11) yields

$$A^{\mathrm{II}}(X,Z) = A^{\mathrm{I}}(X,Z) + A_0 - \sqrt{(\tfrac{1}{2})}\exp\left(-\tfrac{1}{4}\mathrm{i}\pi\right)\{C(u_1)+C(u_2)+\mathrm{i}[S(u_1)+S(u_2)]\}, \tag{2.15}$$

where $C(u)$ and $S(u)$ are the Fresnel integrals

$$C(u) = \left(\frac{2}{\pi}\right)^{\frac{1}{2}}\int_0^u \cos t^2\,\mathrm{d}t, \tag{2.16}$$

$$S(u) = \left(\frac{2}{\pi}\right)^{\frac{1}{2}}\int_0^u \sin t^2\,\mathrm{d}t, \tag{2.17}$$

and

$$u_1 = \frac{\sigma}{(2Z)^{\frac{1}{2}}}(1+X), \quad u_2 = \frac{\sigma}{(2Z)^{\frac{1}{2}}}(1-X), \tag{2.18}$$

$$A^{\mathrm{I}}(X,Z) = 2A_0\frac{\sigma}{(2\pi Z)^{\frac{1}{2}}}\int_{-\frac{1}{2}}^{\frac{1}{2}} \exp\left[\mathrm{i}(\alpha+\beta t+\gamma t^2)\right]\mathrm{d}t, \tag{2.19}$$

$$\alpha = \frac{\sigma^2}{2}\left(1+\frac{X^2}{Z}\right) - \frac{\pi}{4}, \tag{2.20}$$

$$\beta = -\frac{2\sigma^2 X}{Z}, \quad \gamma = \frac{2\sigma^2(1-Z)}{Z}. \tag{2.21}$$

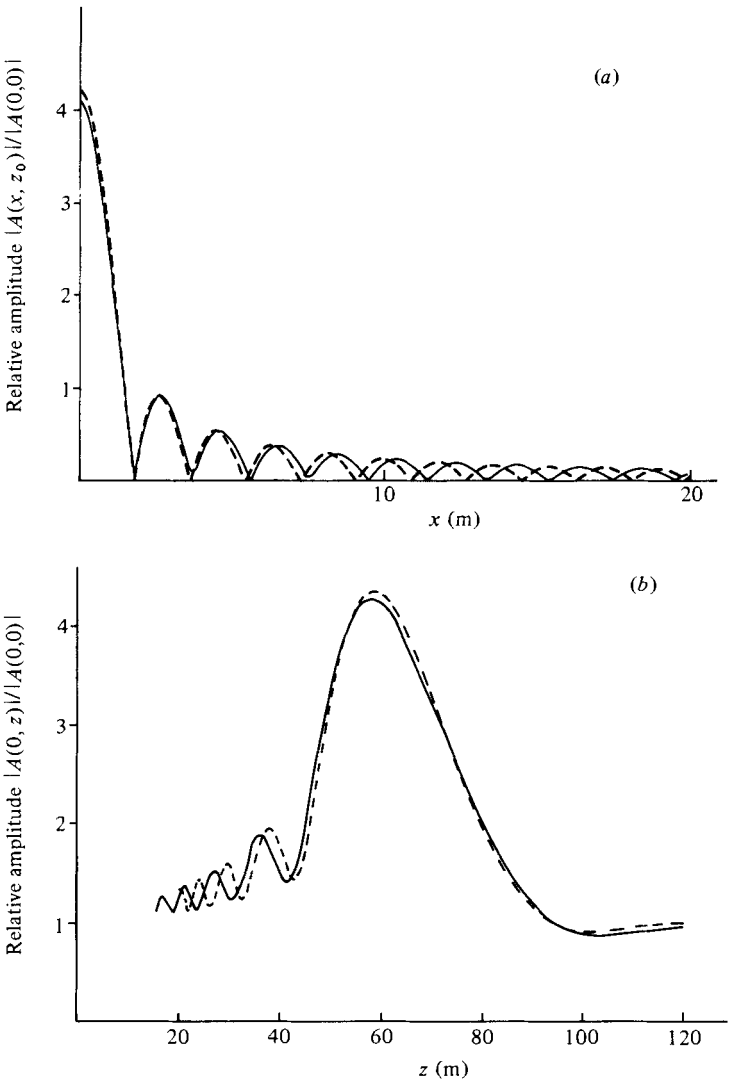

FIGURE 2. Plots of the wave amplitude as computed using the *exact* linear theory ((2.2)–(2.5), solid curve) and the *parabolic* linear theory ((2.19), dashed curve) for observation points on the focal line $z = z_0$ in (*a*) and on the $x = 0$ axis in (*b*). The focusing geometry is the same as shown in figure 1 (*b*), corresponding to $\sigma^2 = 28.805$, and the boundary value is assumed to vanish outside the lens (cf. (2.13)).

The computation of $A^{\mathrm{I}}(X, Z)$ in (2.19) proceeds quickly by means of an algorithm that has been developed specially for that kind of an integral (Stamnes, Spjelkavik & Pedersen 1983). This algorithm involves the Fresnel integrals for values of $|\gamma|$ larger than 0.6; for smaller values of $|\gamma|$, $\exp(\mathrm{i}\gamma t^2)$ is expanded in a Taylor series and each term in the resulting integrand is integrated analytically.

A comparison of the results of the *exact* linear theory ((2.2)–(2.5)) with those of the *parabolic* linear theory ((2.15)–(2.21)) has been made for $\sigma^2 = 28.805$, which corresponds to its actual value in the experiment to be discussed, where $k = 6.283\ \mathrm{m}^{-1}$, $a = 16.585$ m, $z_0 = 60$ m (cf. (2.9)). For case I, in which the boundary

value is zero outside the lens (cf. (2.13)), the results are shown in figure 2(*a*) for observation points on the focal line $z = z_0$, and in figure 2(*b*) for observation points on the $x = 0$ axis. Despite the significant departure from the requirement that $\sigma^2 = O(1)$, the discrepancy between the two theories is seen to be small. Similarly, a comparison of the results of the parabolic linear theory corresponding to cases I and II (cf. (2.13)–(2.14)) shows only small discrepancies. Thus, as far as the linearized theory is concerned, we may conclude that the parabolic theory is quite robust, and that there is no significant difference between the results of cases I and II.

3. Non-linear theory in the parabolic approximation

The parabolic nonlinear theory was first developed by Yue & Mei (1980) for head-sea scattering of slender objects, and can be applied here with minor modifications. The governing equation is the cubic Schrödinger equation

$$\frac{\partial A'}{\partial z} - \frac{\mathrm{i}}{2k}\frac{\partial^2 A'}{\partial x^2} + \frac{\mathrm{i}}{2}K'|A'|^2 A' = 0, \tag{3.1}$$

where A' is the actual amplitude of the wave at the position (x, z), and

$$K' = k^3 \frac{C}{C_g}\frac{\cosh 4kd + 8 - 2\tanh^2 kd}{8\sinh^4 kd} \tag{3.2}$$

with

$$C = \frac{\omega}{k}, \quad C_g = \frac{\partial \omega}{\partial k} = \frac{\omega}{k \sinh 2kd}(\tfrac{1}{2}\sinh 2kd + kd), \tag{3.3}$$

and with d being the depth of the water.

Introducing again the scaled coordinates X, Z, given in (2.8), and also a scaled amplitude

$$A = A'/A_0, \tag{3.4}$$

where A_0 is the amplitude of the wave as it emerges from the lens, we have

$$2\frac{\partial A}{\partial Z} - \frac{\mathrm{i}}{\sigma^2}\frac{\partial^2 A}{\partial X^2} + \mathrm{i}K|A|^2 A = 0, \tag{3.5}$$

$$K = z_0 A_0^2 K' = k z_0 (k A_0)^2 \frac{K'}{k^3}, \tag{3.6}$$

where K' is given in (3.2).

The cubic nonlinear Schrödinger equation (3.5) is solved for the same boundary values as in (2.13) and (2.14). To remove small rapid oscillations in the numerical solutions, the jump at $X = \pm 1$ in the boundary value is smoothed over a few X-steps (ΔX). The numerical technique used is a nonlinear variant of the method due to DuFort & Frankel (1953), which is employed in favour of the scheme of Yue & Mei (1980) to minimize numerical oscillations in the solutions:

$$A_j^{n+1} = A_j^{n-1} + \frac{\mathrm{i}\Delta Z}{\sigma^2 \Delta X^2}(A_{j+1}^n - A_j^{n+1} - A_j^{n-1} + A_{j-1}^n) - \tfrac{1}{2}\mathrm{i}K\Delta Z\,|A_j^n|^2 (A_j^{n+1} + A_j^{n-1}), \tag{3.7}$$

where

$$A_j^{n+1} \approx A((n+1)\Delta Z, j\Delta X), \tag{3.8}$$

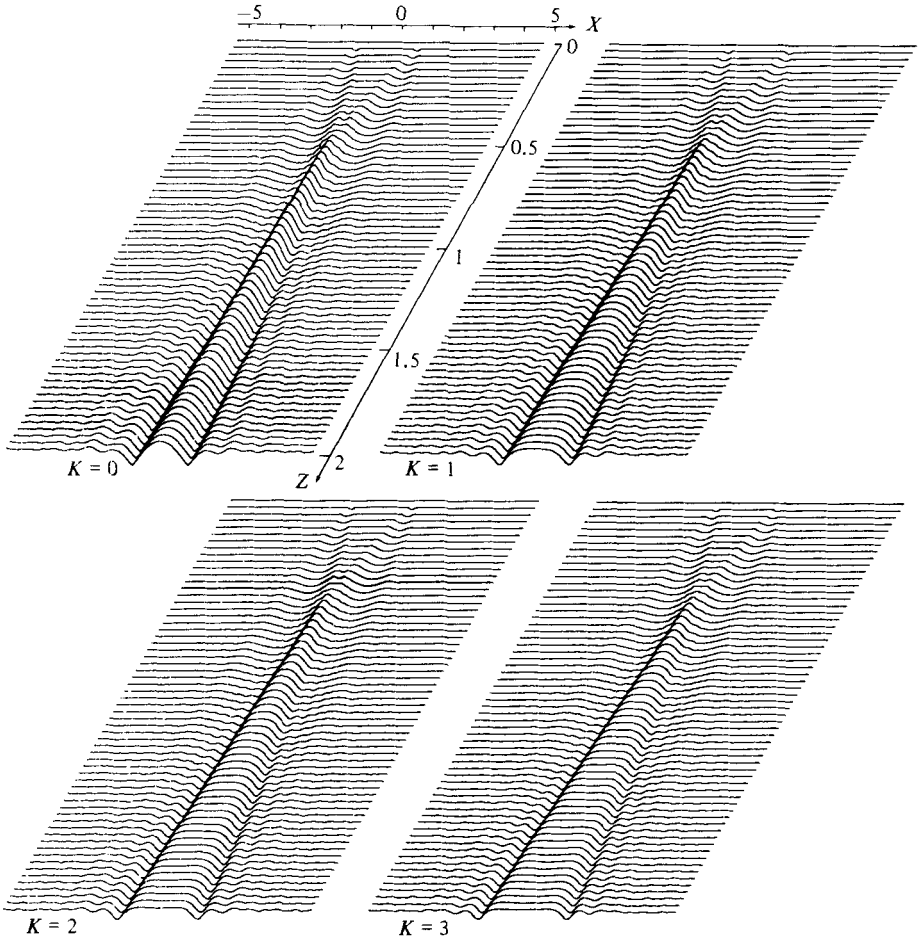

FIGURE 3. Plots of the amplitude distribution $|A(X,Z)|$ for $\sigma^2 = 5$ and $K = 0, 1, 2, 3$ in the region $|X| \leqslant 5$ and $0 \leqslant Z \leqslant 2$. The lens is at $Z = 0$ and the geometrical focal point at $Z = 1$. $|A(X,Z)|$ takes on its maximum value at $Z = 0.83$, 0.72, 0.66 and 0.61, for $K = 0, 1, 2$ and 3 respectively. Thus we have a focal shift towards the lens, which is well known in linear theory ($K = 0$) for small values of σ, but which is amplified because of nonlinear effects. It is seen that nonlinearity tends to broaden and flatten the envelope in the focal region.

and the scheme is implicit. A no-flux boundary condition is applied in the X-direction, i.e.

$$\frac{\partial A}{\partial X} = 0 \quad \left(|X| = \frac{b}{a}\right), \tag{3.9}$$

where $2a$ is the width of the lens, and b is chosen sufficiently large so that the solution is unaffected by further increases in b. A good value for b was found to be $b = 5a$. Alternatively one can require that

$$A = A_0 \exp\left[-\mathrm{i}\tfrac{1}{2}KA_0^2\frac{z}{z_0}\right] \quad (|x| \geqslant b). \tag{3.10}$$

which is the plane Stokes wave. It is computationally easier to use (3.9); the results satisfy (3.10) when $b/a \geqslant 5$.

The numerical scheme of (3.7) has been found to be satisfactory when compared with the analytical parabolic solution of (2.15), in the linearized limit of $K = 0$. To give a preliminary idea of the nonlinear effects, we show in figure 3 the envelope $|A(X, Z)|$ for $\sigma^2 = 5$ and $K = 0, 1, 2, 3$. The geometrical focal point is at $Z = 1$ according to linear ray theory. Because of the small value of σ we observe a focal shift which is well known in linear theory. This shift implies that the maximum value of $A(X, Z)$ is not at the geometrical focal point but is shifted towards the lens. For $K = 0, 1, 2, 3$, $A(X, Z)$ has its maximum value at $Z = 0.83$, 0.72, 0.66 and 0.61 respectively. Thus nonlinear effects tend to increase the focal shift. Also it is seen that nonlinearity tends to broaden and flatten the envelope in the focal region.

4. Evolution of the spectral amplitude in the nonlinear theory

In linear theory the angular spectrum, given by $\tilde{\eta}(k_x, z)$ in the exact theory (cf. (2.4*a*)) or by $\tilde{A}(f_X, Z)$ in the parabolic theory (cf. (2.10*b*)), does not change in magnitude from one line z = constant to another. Physically this means that, when we represent, for example, the wave $\eta(x, z)$ as a superposition of plane waves that propagate in various directions $\boldsymbol{k} = \{k_x, (k^2 - k_x^2)^{\frac{1}{2}}\}$ (cf. (2.4*b*)), then the complex amplitude $\tilde{\eta}(k_x, z)$ of each plane wave only changes its phase, not its magnitude, between two lines z = constant. In nonlinear theory, $|\tilde{A}(f_X, Z)|$ changes with Z, and we can use this change between two lines Z = constant as a measure of nonlinear effects in that region.

Since the angular spectrum at a line z = constant is the Fourier transform of the wave at that line (cf. (2.4*b*) and (2.10*c*)), we see that the magnitude of the Fourier transform of the field does not change with z in the linear theory. For obvious reasons we call this quantity $|\tilde{\eta}(k_x, z)|$ or $\tilde{A}(f_X, Z)|$ the *spectral amplitude* of the field. In regions far from the focal area in figure 1, the field is to a good approximation given by only one of the plane waves in (2.2*b*) or (2.10*a*). This result follows by applying the method of stationary phase to (2.2*b*) or (2.10*a*). Let the focal line be at $z = z_0$, and write (2.4*b*) in the form

$$\eta(x, z) = \int g(k_x)\, \mathrm{e}^{\mathrm{i}\phi(k_x)}\, \mathrm{d}k_x. \tag{4.1}$$

Further assume that $g(k_x)$ varies slowly in comparison with $\exp(\mathrm{i}\phi(k_x))$ for large $r = [x^2 + (z - z_0)]^{\frac{1}{2}}$. Then the method of stationary phase is appropriate. One readily finds the stationary-phase point to be

$$k_x^{\mathrm{s}} = k\frac{x}{r}, \tag{4.2}$$

and further

$$\phi(k_x^{\mathrm{s}}) = kr, \quad \phi''(\kappa_x^{\mathrm{s}}) = -\frac{r^3}{(z - z_0)^2}. \tag{4.3}$$

Substitution into the stationary-phase formula yields

$$\eta(x, z) \sim \frac{\exp(-\frac{1}{2}\mathrm{i}\pi)}{(2\pi)^{\frac{1}{2}}}\, \tilde{\eta}\left(k\frac{x}{r}, 0\right)\frac{z - z_0}{r}\frac{\exp(\mathrm{i}kr)}{r^{\frac{1}{2}}}. \tag{4.4}$$

Thus, at large distances r away from the focus, the field is *locally* a plane wave $\exp(\mathrm{i}kr)\, r^{\frac{1}{2}}$ with amplitude $\tilde{\eta}(kx/r, 0)$. Therefore, far from the focus, the spectral amplitude is a direct measure of the directional distribution of the energy flux. Since the spectral amplitude remains constant in the linear theory, the directional distribution of the energy flux is the same before focusing the wave as after.

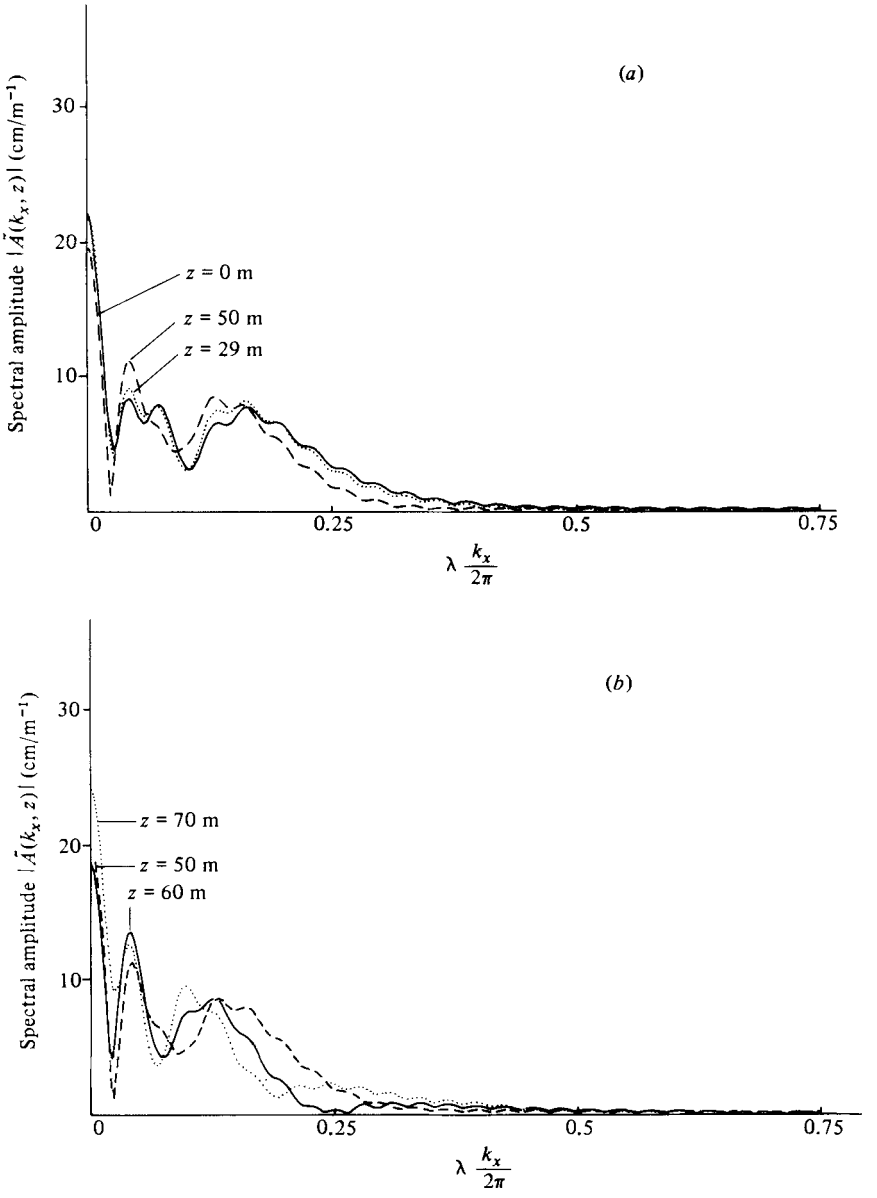

FIGURE 4(*a*, *b*). For caption see facing page.

In the nonlinear theory the principle of superposition no longer holds. Thus, if we compute the Fourier transform of the wave at line z = constant, we can no longer associate it with the complex amplitude of a single plane wave. However, if the nonlinearities are weak, as will be the case in regions far from the focus, we can to a good approximation claim that the spectral amplitude (the magnitude of the Fourier transform) represents the magnitude of the corresponding plane wave, and also that it is a good measure of the directional distribution of energy.

From the considerations above it is clear that one may obtain a measure of nonlinear effects by considering the evolution of the spectral amplitude in nonlinear theory: the larger the nonlinearities, the larger the change of the spectral amplitude between two lines z = constant.

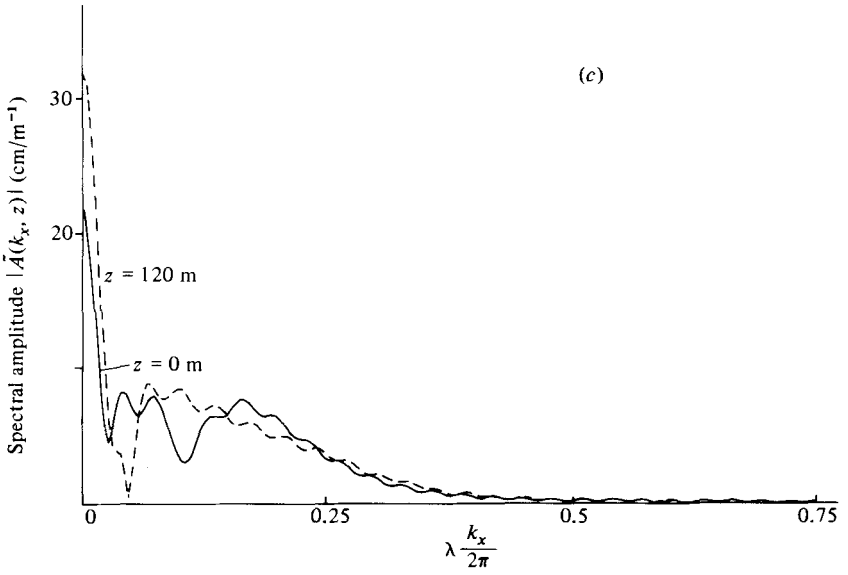

FIGURE 4. Plots of the spectral amplitude $|A(k_x, z)|$ according to nonlinear theory ((3.5) with $K = 1.55$ and (3.9) and (4.2)) on different lines z = constant in the region between $z = 0$ (i.e. at the position of the lens in figure 1 (*b*) and $z = 120$ m (i.e. one focal distance beyond the geometrical focus in figure 1 *b*). The change in the spectral amplitude between two lines z = constant is a direct measure of the strength of nonlinear effects in that region.

Using unscaled coordinates, we have for the angular spectrum in the parabolic theory (linear or nonlinear)

$$\bar{A}(k_x, z) = \int_{-\infty}^{\infty} A(x, z) \exp(-\mathrm{i}k_x x)\, \mathrm{d}x. \tag{4.5}$$

We now restrict our attention to case II (cf. (2.14)). Then, according to the solution of §3, the field is a plane Stokes wave for $|x| \geqslant b$. Using (3.10), we may rewrite (4.5) as follows:

$$\bar{A}(k_x, z) = \int_{-b}^{b} A(x, z) \exp(-\mathrm{i}k_x x)\, \mathrm{d}x + bA_0 \exp\left[-\mathrm{i}\frac{1}{2}\frac{KA_0^2 Z}{z_0}\right]\left\{\delta\left(\frac{bk_x}{2\pi}\right) - 2\,\mathrm{sinc}\,(bk_x)\right\}, \tag{4.6}$$

where $\delta(x)$ is the Dirac delta function and $\mathrm{sinc}\,(x) = \sin(x)/x$. The integral in (4.6) may be computed efficiently by the use of a fast-Fourier transform (FFT) algorithm.

In the linear parabolic theory, the spectral amplitude is obtained by substituting (2.14) into (2.10*b*). The result is

$$\bar{A}(k_x, z = 0)\, aA_0\left\{\delta\left(\frac{ak_x}{2\pi}\right) - 2\,\mathrm{sinc}\,(ak_x) + 2\int_{-\frac{1}{2}}^{\frac{1}{2}} \exp[\mathrm{i}(\alpha + \beta t + \gamma t^2)]\, \mathrm{d}t\right\}, \tag{4.7}$$

where

$$\alpha = \tfrac{1}{2}\sigma^2, \quad \beta = -2ak_x, \quad \gamma = -2\sigma^2. \tag{4.8}$$

The integral in (4.7) may be computed efficiently by means of the algorithm that is described after (2.21).

As a check on our implementation of the FFT algorithm, we first computed $\bar{A}(k_x, z = 0)$ from (4.7). Then we computed it by substituting $A(x, 0)$ from (2.14) into

(4.8) with $b = 5a$ and employing the FFT algorithm. The spectral amplitudes $|\tilde{A}(k_x, z = 0)|$ resulting from these two computations were identical.

Next we substituted the solution $A(x, z = \text{constant})$ of (3.5) into (4.2) and used the FFT algorithm to compute $\tilde{A}(k_x, z)$. In these computations the values of σ and K were similar to those in the experiment i.e. $\sigma^2 = 28.805$, $K = 1.55$ (cf. (2.9) and (3.6) with $k = 6.283\ \text{m}^{-1}$, $a = 16.585$ m, $z_0 = 60$ m, $A_0 = 0.725$ cm, $d = 3$ m) (wave steepness $kA_0 = 0.0455$). The results, which are displayed in figure 4, show how the spectral amplitude $|\tilde{A}(k_x, z)|$ changes with z in the nonlinear case.

We would of course expect that the nonlinear effects play the largest role in the focal region, where the wave amplitude is large, and that their influence is small far away from the focal region. The results presented in figure 4 agree well with our expectations. Figure 4(*a*) shows the change in the spectral amplitude over the distance from $z = 0$ to $z = 50$ m. We see that from the line $z = 0$ to the line $z = 29.25$ m, there is practically no change. Thus linear theory is adequate to describe the propagation between the lens and the line $z = 29.25$ m. This fact is utilized in § 5.5. In contrast, the change in the spectral amplitude is quite pronounced as we pass through the focal region from the line $z = 50$ m to the line $z = 70$ m (figure 4*b*). Beyond the line $z = 80$ m the change in $|A(k_x, z)|$ is again smaller, and beyond $z = 110$ m there is practically no change. Thus we may conclude from our findings that for $z < 29.5$ m or $z > 110$ m the linear theory is adequate.

A comparison of the spectral amplitude at $z = 0$ and $z = 120$ m (figure 4*c*) shows that the overall effect of the nonlinearities in the parabolic focusing problem is to cause a directional redistribution of the energy flux. We see that $\tilde{A}(k_x = 0, z = 120\ \text{m})$ is much larger than $\tilde{A}(k_x = 0, z = 0)$, which according to our earlier discussions means that the energy flux is considerably more peaked in the forward direction after passage through the focal region.

5. The experiment

Before describing the experimental procedure and the processing of the experimental data in detail, we give a brief explanation of the essential steps.

The wave field is recorded simultaneously in 72 positions on a line $z = \text{constant}$ in the measurement area in figure 1(*b*) by means of an array of pressure transducers. The spacing between the transducers is 0.5 m. Stationarity of the wave field is assumed in a measurement period, during which the transducer array is moved through the measurement area shown in figure 1(*b*), and recordings are taken at successive lines $z = \text{constant}$ with a spacing of 0.5 m. An estimate of the wave amplitude right behind the lens, at the line $z = 0$ in figure 1(*b*), is obtained from simultaneous measurements of the wave by a two-dimensional array of pressure transducers. The height of the incident wave may change during the scanning of the measurement area, and we use this estimate to normalize it. This array, which consists of 3×6 transducers, is placed about 50 wavelengths away from the wavemaker. Because of structural obstructions, no probes were placed immediately behind the lens until at the line $z = 29.25$ m.

The signal recorded by each pressure transducer is stored on magnetic tape for subsequent processing. The objective of the processing is to obtain the wave front at the frequency of the wave generator at each recording line $z = \text{constant}$. To that end, one first uses a FFT algorithm to estimate the temporal Fourier component of the recorded signals at the frequency of the wavemaker. Then one may again employ a FFT algorithm to compute the angular spectrum of the field at a given recording

line z = constant, and use spatial frequency filtering to remove wave components that are due to reflections from the walls of the basin. This is simply done by suppressing that part of the angular spectrum for which the spatial frequency $|k_x|$ is larger than $0.5k$, and it implies that every plane wave is removed whose direction of propagation makes an angle larger than 30° with the z-axis in figure 1 (*b*). (As shown in figure 4, the energy content of the angular spectrum is negligible for $|k_x| \geqslant 0.5k$.) The inverse Fourier transform is then applied to the filtered spectrum to obtain the processed wave.

5.1. *The experimental set-up*

Figure 1 shows the experimental set-up in the basin. The waves incident upon the lens are generated by a conically shaped wavemaker. It oscillates vertically on a cylindrical shaft along the cone axis with its apex pointing downwards. The diameter of the cone at the mean water level is 4 m, and the cone angle is 30°. To eliminate reflections the basin is lined with a wave-damping beach which is made of corrugated aluminium plates with ridges of corrugation perpendicular to the shore. The slope of the beach near the water surface is less than 1:10, and the beach stretches more than 7 metres into the water. Reflections from the shore were never seen to influence the measurements.

The wavemaker generates higher-harmonic components which interact nonlinearly in its near zone. But, at a distance of about 50 wavelengths, these higher harmonics are negligible (see bottom of figure 5) because of their faster rate of radial attenuation (at large distances r from the wavemaker the nth harmonic goes as $(nkr)^{-\frac{1}{2}}$ for $n = 2, 3, 4, \ldots$).

To measure the wave height we use piezoresistive pressure transducers, which in our application have a resolution better than 0.1 $\mathrm{mmH_2}$. The point of measurement of each probe is adjusted to be at 70 mm below the mean water level. This point is located at the end of a steel tube, 2 mm in diameter, which is connected to the pressure-sensitive surface of the transducer by stiff tubing filled with water. Each measurement probe has a resonance frequency above 20 Hz, while the cutoff frequency of the anti-aliasing filter of the recording system is about 4 Hz. The frequency of the wavemaker movement is 1.25 Hz with less than 10% harmonic distortion.

A total number of 90 probes are used in the experiment. 72 probes are placed on a movable boom, which is parallel to the x-axis in figure 1 (*b*). The spacing between the probes on the boom is 0.5 m. To scan out the measurement area in figure 1 (*b*), one displaces the boom parallel to itself and records the wave height at successive lines z = constant with a spacing of 0.5 m. The remaining 18 probes are placed in front of the lens in a two-dimensional array of 3×6 elements, and constitute a phased array which is focused on the wavemaker. The records are used to check that the wave crests are circular arcs centred at the wavemaker.

5.2. *Error sources and calibrations*

The experimental set-up is designed so as to ensure maximum reliability in the measurement of the wave height in the measurement area in figure 1 relative to the wave height of the wave produced by the wavemaker. Therefore all wave-height measurement probes are identical, have identical mountings, and their signals are recorded in identical manners. The point of measurement of each probe is positioned to within ± 0.5 mm around a common depth of 70 mm below the mean water level. Assuming linear waves with a wavelength of 1 m, we find that this uncertainty in

the depth positioning leads to an uncertainty in the measurement of the wave height of less than 1 %. The lens in figure 1 consists of horizontal plates, whose depths have been positioned to the same accuracy of ± 0.5 mm.

To monitor the water level in the basin, one uses electrical conduction probes with a resolution of 0.1 mm in a region of 100 mm above and below the mean water level. The uncertainty in the position of the boom is $\Delta z = \pm 3$ cm.

Each recording is controlled by an accurate clock pulse from one of the computer processors. The movement of the wavemaker is controlled by a microprocessor, while the data logging is managed by a mini-computer. These have separate clocks. Each recording lasts 102.4 s and contains 1024 samples. The recordings that constitute one time sample of each of the 90 transducers are made sequentially in a sampling period of less than 0.1 s, and are time-shifted in the data processing to compensate for the sequential scanning of the data channels.

In practice, it turns out, however, that the accuracy of the experiment is not limited by technical specifications, as listed above. Instead it is determined by environmental factors like winds and currents in the basin. Also, algal growth sometimes is the cause of defects in transducers. Winds have three major effects. First, wind-driven waves produce noise waves in the basin. Secondly, a steady wind gives rise to a current in the basin, which in turn causes a Doppler shift on the wave field produced by the wavemaker. And, thirdly, stronger winds generate seiches in the basin that cause fluctuations in the water level at each pressure transducer, thus modulating its sensitivity as a wave height probe. This third effect, however, is so weak that it plays a role only in cases in which the experiment already has been spoiled by currents in the basin. In §§5.4 and 5.5 we discuss measures taken in the data processing to reduce effects of winds and currents.

5.3. *The validity of the stationarity approximation*

A typical phenomenon in the nonlinear propagation of gravity waves is the Benjamin–Feir instability, according to which a wave spectrum develops sidebands, causing a modulation of the wave. Similar effects have been seen in this focusing experiment at large amplitudes. Therefore we would like to determine to what extent these effects influence our assumption of a stationary wave field. Figure 5 shows the amplitude spectrum of the 102.4 s time series of one of the transducers as it moves through the focal region on a line parallel to the optical axis of the lens. The focal point is approximately 60 m from the lens. It is evident that sidebands appear as the waves are passing through the focal region. But the influence on the amplitude estimate in the focal region is less than a few percent, and the typical form of the waves in this region is maintained.

Other phenomena which may limit the validity of the stationarity approximation, are small, more or less random currents in the basin. Such currents may be due to wind or convection in the water. In our experiment they give rise to a Doppler shift of the observed wave frequency when the wave passes over a transducer. The effect of this shift may be interpreted as a change in the index of refraction. To obtain an estimate of the uncertainty in the position of the focus, we investigate how such random currents may influence the propagation of the wave. This is done by using a gradient index ray tracing program to show how the associated refractive index alters the form and position of the focal area.

To explain the observed Doppler shift and its equivalent refractive-index change, we consider a transducer at rest in a stationary monochromatic wave field of frequency ν and phase velocity c. In the linear theory we may decompose this wave

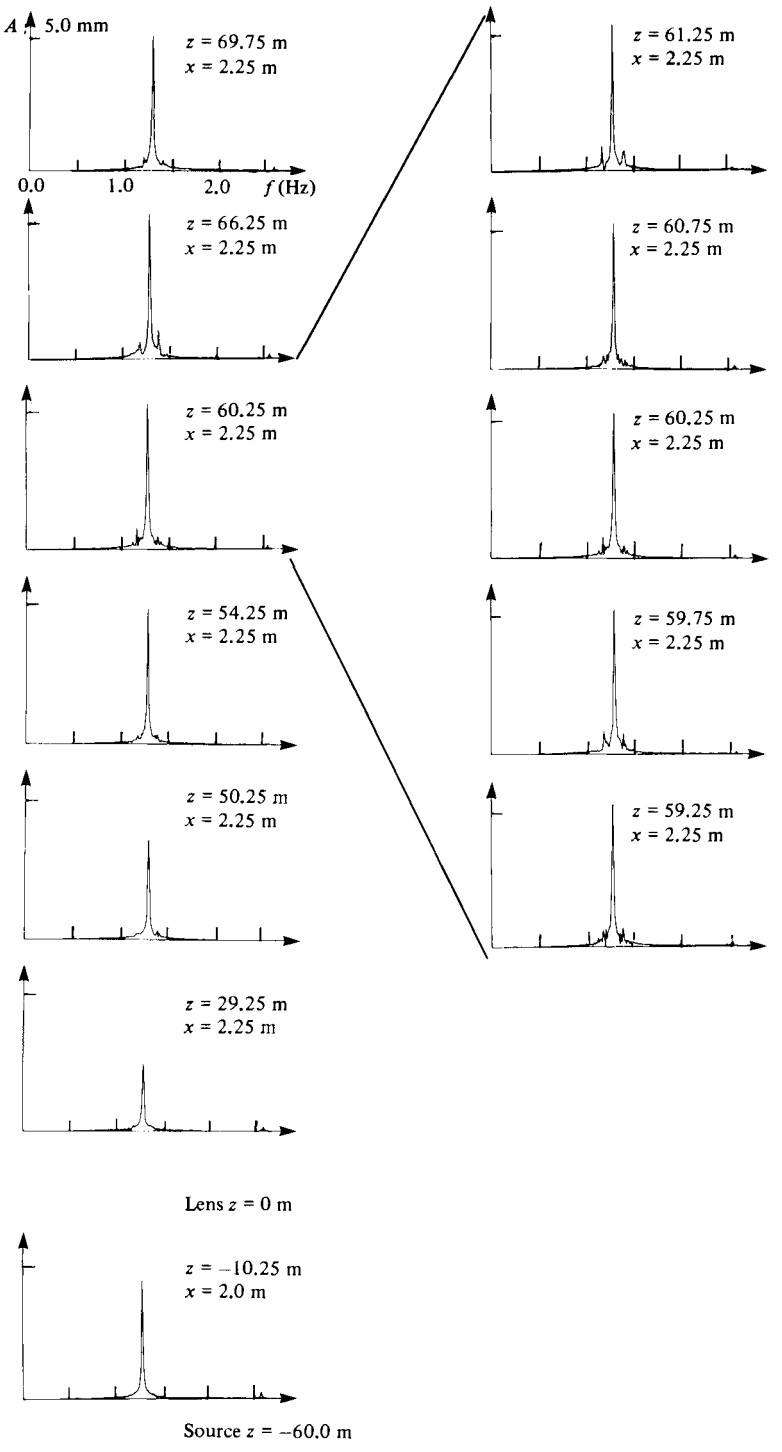

FIGURE 5. Illustration of the Benjamin–Feir instability. The figure shows the frequency spectrum of the wave at different positions (x, z) in the test basin (cf. figure 1 *b*). Sidebands are seen to develop as the wave passes through the focal region.

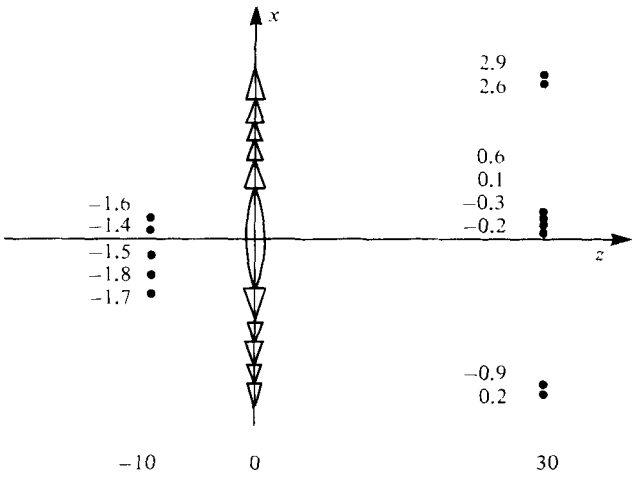

FIGURE 6. Simultaneously measured Doppler shifts at different positions in the test basin. The values of the shifts are given per mile relative to the mean frequency.

field into an angular spectrum of plane waves (cf. (2.2*b*)), and it therefore suffices here to consider one single plane wave. The phase velocity c is the speed with which wave crests pass the transducer, i.e. $c = \lambda/T$, where the wavelength λ and the period T are respectively the distance between two neighbouring wave crests and the time that elapses between their passage over the transducer.

Suppose now that a stationary current of velocity $\boldsymbol{v}$ makes the water drift by the transducer. Then the speed c' by which wave crests pass the transducer is

$$c' = c + v\cos\theta, \quad \cos\theta = \hat{\boldsymbol{n}}\cdot\hat{\boldsymbol{v}},$$

where $\hat{\boldsymbol{v}}$ and $\hat{\boldsymbol{n}}$ are unit vectors in the direction of the current and in the direction of propagation of the plane wave respectively. The observed period is $T' = \lambda/c'$, corresponding to a frequency $\nu' = c'/\lambda$ and a relative Doppler shift

$$\Delta\nu/\nu = (\nu' - \nu)/\nu = c'/c - 1.$$

In the absence of currents we define the index of refraction by $n(x,z) = c(x,z)/c_0$, where c_0 is the phase velocity of the wave in water of infinite depth, and $c(x,z)$ is the (depth-dependent) phase velocity at the position (x,z). Similarly, in the presence of a current, we define the refractive index as $n'(x,z) = c'(x,z)/c_0 = n(x,z)\,[c'(x,z)/c(x,z)]$. The relation between the relative Doppler shift $\Delta\nu/\nu$, caused by the current in the basin, and the relative refractive index change $\Delta n/n$ is thus

$$\frac{\Delta\nu}{\nu} = \frac{c'}{c} - 1 = \frac{n}{n'} - 1 = -\frac{\Delta n}{n'} \approx -\frac{\Delta_n}{n}.$$

Note that n', strictly speaking, depends on the angle between the direction of propagation $\hat{\boldsymbol{n}}$ of the plane wave and the direction $\hat{\boldsymbol{v}}$ of the current.

Figure 6 gives the Doppler shift per mile relative to the measured frequency of the wavemaker at different transducer positions in a sample of several recordings. Since the whole experiment took about 8 h during which the frequency shift might have changed, our estimate is only representative and not exact. The currents may cause a displacement of the focal region, particularly in the transverse direction. To give an explanation of this transverse displacement, we use ray-tracing techniques and the Doppler shifts observed in figure 6. The maximum relative frequency difference

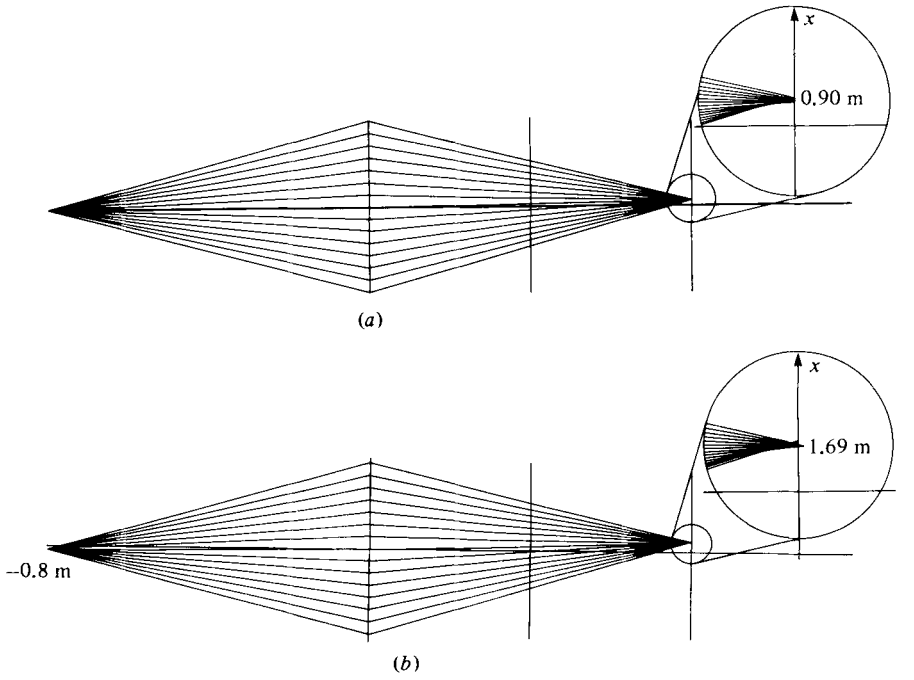

FIGURE 7. Illustration of the sideways displacement of the focal area that may occur if there is a shear current in the basin between the lens and the focus. As explained in the text, the effect of the current may be analysed in terms of an equivalent gradient index medium. Ray traces through the equivalent gradient index medium are shown in (*a*) and (*b*) for the cases in which the wavemaker is positioned on-axis and −0.8 m off-axis respectively.

in the recording is approximately 0.5 %. We assume that this difference is due to a shear current that runs parallel to the optical axis with a speed that decreases linearly from a maximum value at one end of the lens to zero at the optical axis and then increases again to the same maximum speed in the opposite direction at the other end of the lens.

We now make the simplifying assumption that n' does not depend on $\cos\theta = \hat{\boldsymbol{n}}\cdot\hat{\boldsymbol{v}}$, i.e. as far as the computation of n' is concerned we assume that the wavefront emerging from the lens in figure 6 is parallel to the lens and hence to the direction of the assumed current. As a result, we have a phase velocity for the stationary wave field that varies linearly in the direction transverse to the optical axis. Thus, in our ray-tracing model we assume that the index of refraction varies linearly in the x-direction behind the lens in figure 6, with a minimum value of 0.995 at $x = +16.585$ m, corresponding to one edge of the lens, and a maximum value of 1.005 at $x = -16.585$ m, corresponding to the other edge of the lens. As a further simplification, we assume that there are no currents between the wavemaker and the lens and that the lens is perfect in the sense that it transforms the incident diverging circular wavefront into a converging circular wavefront with focus at the geometrical image point. If the wavemaker is situated off-axis in figure 6, then the geometrical image point is the intersection point between the image line $z = 60$ m and the line from the wavemaker through the centre of the lens.

To determine how the gradient index medium behind the lens displaces the focal point we use an algorithm for ray tracing in inhomogeneous media to trace rays through it. As a starting point for this ray trace we make use of the assumption

mentioned above, that just behind the lens the rays are directed towards the geometrical focal point. However, as the rays progress towards the image area they are bent because of the variation in the refractive index. The results of such ray traces are shown in figures 7(*a*) and (*b*) for the cases in which the wavemaker lies respectively on-axis and −0.8 m off-axis. We see that the assumed current distribution tends to displace the position of the focal point approximately 1 m sideways. In addition the gradient index medium is seen to introduce aberrations, which contribute additional uncertainty, as far as an accurate positioning of the image point is concerned. However, from figure 7(*a b*) we can conclude that the image is shifted sideways a distance of about 1.3 m, due to the assumed current distribution behind the lens. Thus, in the actual experiment, where the wavemaker was situated at $x = -0.8$ m, we would expect the image to lie in the region between $x = -0.5$ m and $x = 2.1$ m. In field applications, natural currents can also displace the focal area and affect wave power operation. For a swell of 10 s period, a current of maximum velocity of 0.1 m/s at the tip of the lens can give a comparable displacement of the focal point relative to the wavelength for this simple, but impractical, lens geometry.

5.4. *Processing and noise reduction*

The main objective of the signal processing is to obtain from the experimental data a wave field that is as close as possible to a stationary monochromatic one. In addition, processing is employed to make the wave field as insensitive as possible to noise in the electronics or due to winds, currents and spurious waves in the basin. The details of the processing procedure are given in the appendix.

5.5. *Estimation of the wave at the lens*

To determine the amplitude and phase of the circular wave generated by the wavemaker at its main frequency we use a phased array of 3×6 transducers, which are placed between the wavemaker and the lens in figure 1 (*b*). By processing the data from this array in the right way, one suppresses waves that are reflected from the lens and the walls of the basin, and other spurious waves. The phased array thus provides us with a method for determining the wave generated by the wavemaker, without making any assumptions about the wavemaker and its movement. However, we use the recorded wavemaker signal to check its stability, and by comparisons between the estimated wave at the wavemaker and the recorded signal we can check if the wave generated by the wavemaker is distorted by winds or currents. In the phased-array calculations, one uses the narrowband stationary signal that is obtained by processing the recorded signal as explained briefly in §5.4 and more fully in the appendix. Thereby one supresses noise that falls outside the spectral window employed in the spectral-estimation method given in the appendix. It is beyond the scope of this paper to explain in detail how the phased array works. The details may be found in Løvhaugen (1981*b*).

The height of the incident wave may change during the scanning of the measurement area in figure 1 (*b*). Therefore, we use the estimated wave height, as determined by the phased array, to normalize the incident wave height.

In order to specify the initial data along $z = 0$,† one needs to obtain an estimate of the wave amplitude right behind the lens based on measurements at $z = 29.25$ m; this is done in the following manner. We first assume that the lens is perfect in the sense that it creates a converging circular wave whose relative amplitude distribution

† We could have chosen to regard $z = 29.25$ m as the initial line.

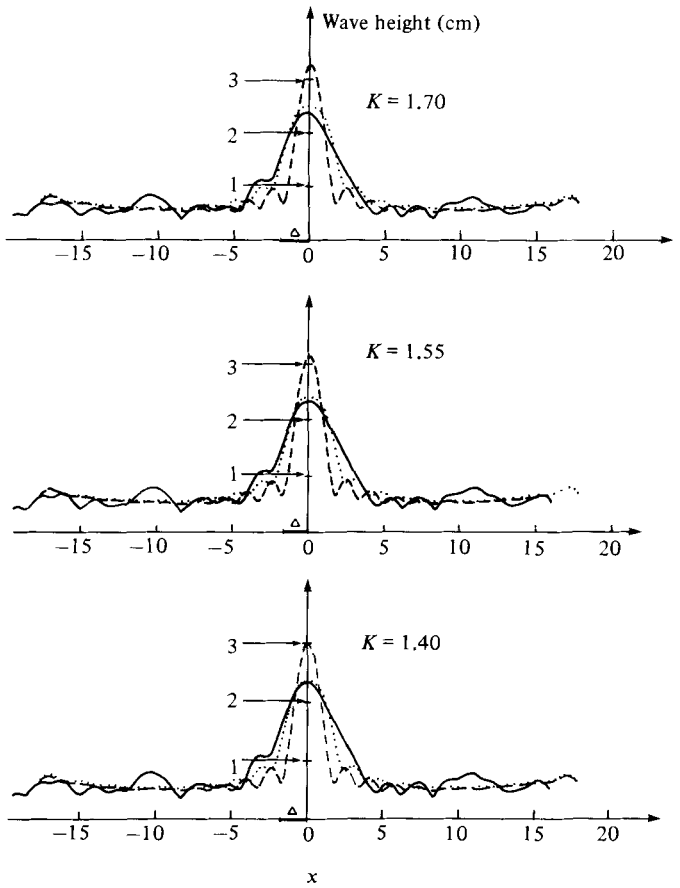

FIGURE 8. Wave heights on the line $z = 60.25$ m, according to linear theory (2.15), dashed curves, nonlinear theory (3.5) and (3.9), dotted curves, and experiment (solid curves). The three different values of the nonlinearity parameter K (cf. (3.5), (3.6)) were obtained from the measured data as explained in the text. The experimental curves are shifted a distance Δ in the x-direction to obtain the best fit with the theories. As explained in the text, the shifts Δ are probably caused by wind-generated currents in the basin.

across the aperture is the same as for the incoming diverging circular wave. The reference amplitude A_0 at $(0, 0)$ is found by assuming that the linear theory is a good approximation between the lines $z = 0$ and $z = 2.25$ m. By equating the theoretical energy flux at $z = 29.25$ m to the energy flux implied from the measurements, we find A_0. Several measurements were made along lines slightly behind $z = 29.25$ m. From them we infer that $A_0 = 7.25 \pm 0.3$ mm. The corresponding K-values are $K = 1.55 \pm 0.15$ (cf. (3.6)).

The initial condition for the nonlinear calculation is in the form of (2.14). In the experiments the waves outside the aperture were diverging circular waves, but this discrepancy should not affect a region not too far from the optical axis (see the last sentence of §2).

6. Comparison between experimental and theoretical results

Comparisons between experimental results, recorded and processed as described in §5, and results of parabolic linear theory ((2.15)) and parabolic nonlinear theory

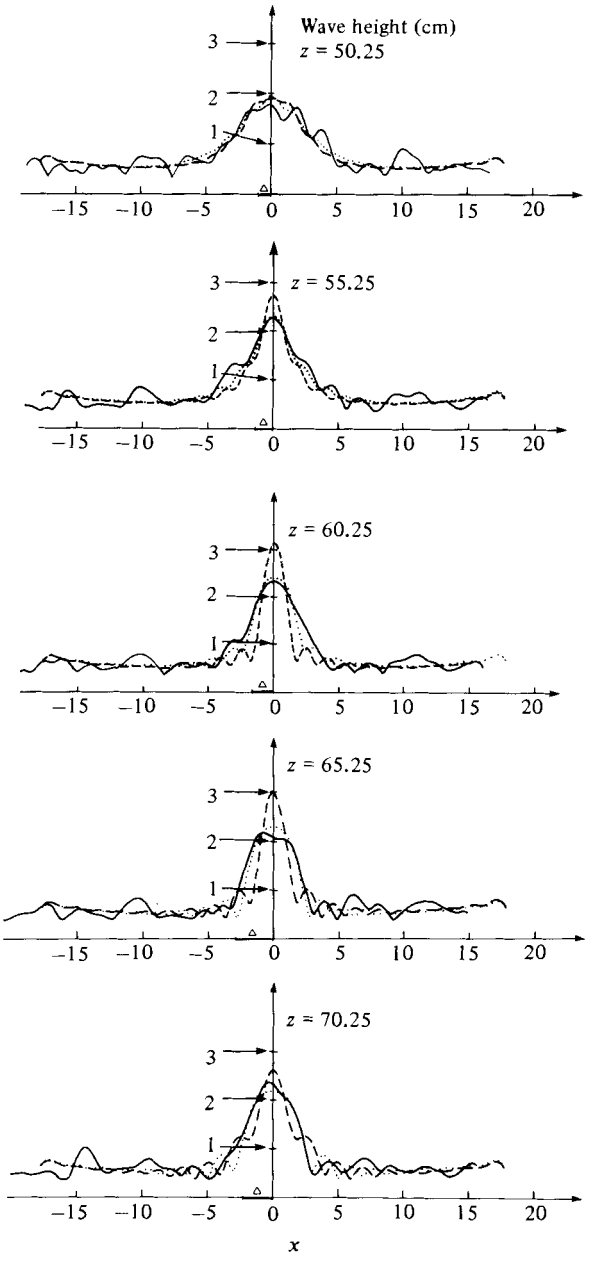

FIGURE 9. Comparisons between wave heights according to linear theory (2.15), dashed curves), nonlinear theory (3.5) with $K = 1.55$ and (3.9), dotted curves), and experiment (solid curves) at different lines z = constant (cf. figures 1 (*b*) and 8). The shift Δ is as explained in the legend on figure 8.

((3.5) and (3.9)) are presented in figures 8–10. The theoretical results pertain to a lens surrounded by deep water (case II) with initial data as specified in (2.14). The amplitude A_0 (cf. (3.4)) right behind the lens in figure 1 (*b*) is estimated on the basis of the measured data in the manner explained at the end of § 5.

In figure 8, relative wave heights are plotted as obtained from the measured data

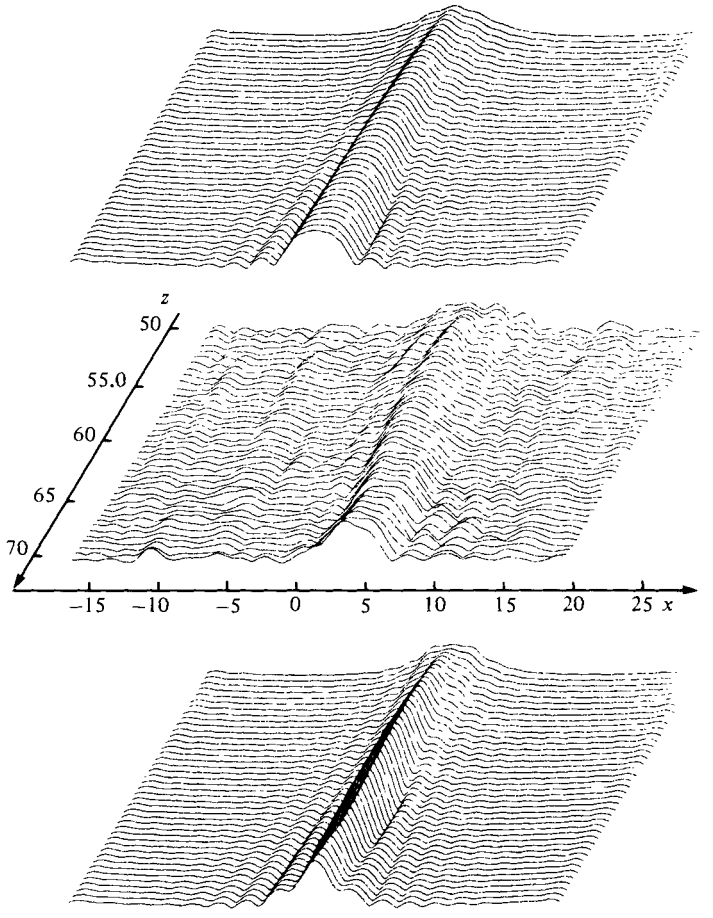

FIGURE 10. Comparison between the measured amplitude distribution and the distributions predicted by linear and nonlinear theory in the measurement area. The upper and lower figure show respectively the results of *nonlinear* theory ((3.5) with $K = 1.55$ and (3.9)) and *linear* theory ((2.15)), and the figure in between shows the results obtained in the experiment. The geometry is the same as in figure 1 (*b*).

(solid curves), from the linear theory (dashed curves), and from nonlinear theory (dotted curves). Each experimental curve is shifted a distance Δ in the x-direction to obtain a best possible fit between the results of theories and experiment. As explained in §5.3, the shift may be caused by wind-generated currents in the basin.

We see from fig. 8 that the nonlinear theory agrees much better with experiment than does the linear theory. It is also apparent that the agreement between nonlinear theory and experiment is little affected by changes in the value of the nonlinearity parameter K within its estimated limits (cf. the discussion at the end of §5.5).

Figure 9 shows the same kind of plots as in figure 8, but in this case the nonlinearity parameter K is constant, i.e. $K = 1.55$, while the distance $z - z_0$ from the geometrical focus at $z_0 = 60$ m varies from one plot to another. We see that far from the focus on the incident side, i.e. at $z = 50.25$ m, the difference between the three curves is small. As focus is approached, the deviation increases between linear theory on one hand and nonlinear theory and experiment on the other hand, and this deviation is maintained throughout the measurement area.

In figure 10, three-dimensional plots are shown of the relative wave heights according to linear theory (lower figure), nonlinear theory with $K = 1.55$ (upper figure), and experiment. Apart from small asymmetries and a bending of the Z-axis in the experimental plot (which, as discussed earlier, may be caused by wind-generated currents in the basin) we again see a striking similarity between the results of nonlinear theory and experiment.

7. Summary

In this paper we have compared experimental results obtained by focusing relatively large-amplitude water waves with results of linear and nonlinear theories. Our findings may be summarized as follows.

By comparing the results of the *exact* linear theory with those of the *parabolic* linear theory, we have established that the parabolic theory is adequate to describe the focusing geometry in figure 1 (*b*), in which the convergence angle is as large as $\theta_0 = 15°$. We also have found no significant difference in the results whether the lens in figure 1 (*b*) is placed in the open sea or fills a hole in a breakwater.

The change in the spectral amplitude from one line $z =$ constant to another is a quantitative measure of the role of nonlinear effects. As expected, the nonlinear effects are found to be largest in the focal region. The overall effect of the nonlinearities is to make the energy flux much more peaked in the forward direction after the wave has passed through the focal area.

The amplitude variations according to the nonlinear theory compare well with those of experiments, while there is some discrepancy between the results of linear theory and experimental results. The slight tilt of the axis (cf. figure 10) is attributed to possible wind-induced currents in the basin.

As a result of the nonlinear effects, the transverse extent of the focal area is about 1.5–2 times as large as one would predict from linear theory. Since, however, the transverse extent of the focal area is still very small compared to the size of the lens, the efficiency of the lens as an energy concentrator is not significantly deteriorated by the nonlinear effects.

In these experiments the waves were generated from a point source; the wave-steepness just behind the lens was rather small, $kA_0 = 0.0455$. In coastal applications the incident waves are more likely plane and the steepness can be much larger, so that nonlinearity may lead to breaking in the focal region. Such a strong nonlinearity is beyond the scope of the present study.

We would like to thank E. Mehlum for making this work possible and for useful discussions on several topics of the paper. Also, we thank K. Løvaas and S. Ljunggren for conducting the experiment and H. Heier for providing the ray traces in figure 8. Support of this research was provided by the Royal Norwegian Ministry of Petroleum and Energy to the Central Institute for Industrial Research and by the U.S. Department of Energy and the Office of Naval Research to Massachusetts Institute of Technology.

Appendix

In this appendix we present the details of the signal-processing procedure we have applied to the experimental data in order to obtain a wave field that is as close as possible to a stationary, monochromatic one.

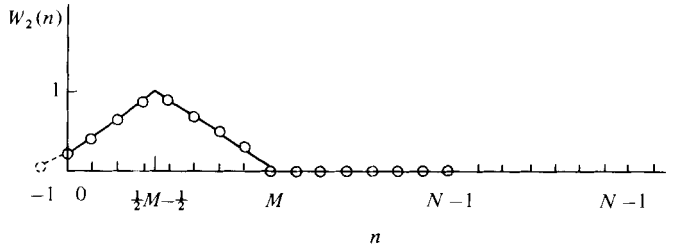

FIGURE 11. Data window used in the estimation of the power spectrum (cf. (A 4)).

As mentioned in the text, a stationary wave field is constructed from separate pressure recordings at 72 different positions on various lines z = constant parallel to the lens (cf. figure 1). Each recording lasts 102.4 s, and the time delay between the recordings at two neighbouring lines z = constant is a couple of minutes.

First, one estimates the power spectrum of each recording, and uses the value of the power spectrum at the frequency of the wavemaker as an unbiased estimate of the wave amplitude at the position in which the recording is made. An estimate of the phase of the recorded signal relative to the phase of the wavemaker signal is obtained by comparing the two periodograms.

Since our aim is to obtain a quasi-monochromatic wave field, one would normally suppress noise by using a narrow-bandpass filter. One could achieve this by using the discrete Fourier transform component at the wavemaker frequency of a recording of a very long duration. However, the observed Doppler shift would make this procedure unreliable. With a recording of 102.4 s duration the spectral window would be so narrow that part of the signal power is likely to fall outside of it.

The best estimate of the energy in the received signal is obtained by integrating the power spectrum under the spectral peak near the wavemaker frequency. However, since this procedure is rather time consuming in practice, a simpler procedure would be desirable. In the search for such a procedure we have tried estimates based on using the peak value of the power spectrum and data windows of different shapes and lengths. In tests performed on the recorded data, comparisons between estimates obtained as just described and estimates obtained by integrating the power spectrum have shown that the use of triangular data windows of 25.6 s duration gives the most stable estimates of the signal energy. In other words, the signal energy estimated by using the peak value of the power spectrum in combination with a triangular data window of 25.6 s agrees well with that obtained by integrating the power spectrum under the spectral peak using a 102.4 s window.

The formula we have used to compute an estimate of the stationary-wave amplitude A at a given observation point is as follows:

$$A = \left[\frac{16}{3}\frac{M(M+2)}{(M+1)^3\Delta t^3} B(f_g^{\max})\right]^{\frac{1}{2}}, \tag{A 1}$$

where the power spectrum $B(f_g^{\max})$ is

$$B(f_g^{\max}) = \frac{1}{K}\sum_{j=1}^{K}\frac{\Delta t}{NU_2}|\mathrm{FFT}\,(s^j(n\Delta t)\,w_2(n\Delta t))|^2, \tag{A 2}$$

with

$$s^j(n\Delta t) = s((j(M-1)+n)\,\Delta t), \tag{A 3}$$

$$w_2(n\Delta t) = \begin{cases} (n+1)\dfrac{2}{M+1} & (n = 0, \ldots, \tfrac{1}{2}M-1), \\ (M-n)\dfrac{2}{M+1} & (n = \tfrac{1}{2}M, \ldots, M), \end{cases} \tag{A 4}$$

$$U_2 = \frac{1}{N}\sum_{n=0}^{N-1} w^2(n) = \frac{M(M+2)}{3N(M+1)}, \tag{A 5}$$

and

$M = 256$ = length of data window,

$N' = 512$ = FFT length,

$\Delta t = 1024$ = length of recording,

$t = 0.1$ s = sampling time,

$K = \dfrac{N'}{M} = 4$ = number of spectra averaged.

The window function $w_2(n)$ in (A 4) is illustrated in figure (11).

The phase ϕ_0 of the narrowband signal is given in terms of the phase θ_0 at frequency f_0 of the averaged periodogram by the formula

$$\phi_0 = \theta_0 - M\Delta t f_0(K-1), \tag{A 6}$$

where M, Δt and K are given above.

REFERENCES

DuFort, E. C. & Frankel, S. P. 1953 Stability conditions in the numerical treatment of parabolic differential equations. *Math. Tables Aids Comput.* **7**, 135–152.

Heier, H. 1981 Two-element holographic lens system for water waves. Theory and measurements. *Central Inst. for Indust. Res., Blindern, Oslo, SI Rep.* 78 04 08-5 (in Norwegian).

Løvhaugen, O. 1981*a* Single holographic lens for water waves. Theory and measurements. *Central Inst. for Indust. Res., Blindern, Oslo, SI Rep.* 78 04 08-4 (in Norwegian).

Løvhaugen, O. 1981*b* Measurements of wave height and energy transport for water waves in an outdoor test basin. *Central Inst. for Indust. Res., Blindern, Oslo, SI Rep.* 78 04 08-3.

Mehlum, E. 1980 A circular cylinder in water waves. *Appl. Ocean Res.* **2**, 171–177.

Mehlum, E. & Stamnes, J. J. 1978 On the focusing of ocean swells and its significance in power production. *Central Inst. for Indust. Res. Blindern, Oslo, SI Rep.* 77 01 38.

Oppenheimer, A. V. & Schafer, R. W. 1975 *Digital Signal Processing*, §11.6.1. Prentice-Hall.

Southwell, W. H. 1981 Validity of the Fresnel approximation in the near field. *J. Opt. Soc. Am.* **71**, 7–14.

Stamnes, J. J. 1981 Focusing of two-dimensional waves. *J. Opt. Soc. Am.* **71**, 15–31.

Stamnes, J. J., Ljunggren, S. & Spjelkavik, B. 1981 Propagation and focusing of linear waves in water of constant depth. *Central Inst. for Indust. Res. Blindern, Oslo, SI Rep.* 78 04 09–3.

Stamnes, J. J., Spjelkavik, B. & Pedersen, H. M. 1983 Evaluation of diffraction integrals using local phase and amplitude approximation. *Optica Acta* **30**, 207–222.

Yue, D. K. P. & Mei, C. C. 1980 Forward scattering of Stokes waves by a thin wedge. *J. Fluid Mech.* **99**, 33–52.